Compositional effects on the growth of Mg(*M*)O films

M. Saraiva,[1,a)] V. Georgieva,[2] S. Mahieu,[1] K. Van Aeken,[1] A. Bogaerts,[2] and D. Depla[1]
[1]*Department of Solid State Sciences, Ghent University, Krijgslaan 281(S1), 9000 Ghent, Belgium*
[2]*Research Group PLASMANT, Department of Chemistry, University of Antwerp, Universiteitsplein 1, 2610 Antwerp, Belgium*

(Received 7 September 2009; accepted 6 December 2009; published online 3 February 2010)

The influence of the composition on the crystallographic properties of deposited Mg(*M*)O (with *M* = Al, Cr, Ti, Y, and Zr) films is studied. For a flexible control of the composition, dual reactive magnetron sputtering was used as deposition technique. Two different approaches to predict the composition are discussed. The first is an experimental way based on the simple relationship between the deposition rate and the target-substrate distance. The second is a route using a Monte Carlo based particle trajectory code. Both methods require a minimal experimental input and enable the user to quickly predict the composition of complex thin films. Good control and flexibility allow us to study the compositional effects on the growth of Mg(*M*)O films. Pure MgO thin films were grown with a (111) preferential out-of-plane orientation. When adding *M* to MgO, two trends were noticed. The first trend is a change in the MgO lattice parameters compared to pure MgO. The second tendency is a decrease in the crystallinity of the MgO phase. The experimentally determined crystallographic properties are shown to be in correspondence with the predicted properties from molecular dynamics simulations. © *2010 American Institute of Physics*. [doi:10.1063/1.3284949]

I. INTRODUCTION

As discussed by Willmott,[1] most of the new technological interesting materials have a complex chemical and crystalline structure. A similar message to the scientific community is given by Plummer *et al.*[2] An example of the increased complexity is the use of the complex metal oxide thin films. These coatings find application as corrosion and wear resistant coatings,[3,4] high-*k* dielectrics,[5,6] solid state ionic conductors in solid oxide fuel cells,[7–10] or thin film batteries.[11–13] As one of the future challenges for the thin film deposition, Willmott and others see the control required for the composition of complex metal oxides.[1,14] Indeed, exact control of the independent dosing of the individual metallic elements is still very problematic. Nevertheless, the stoichiometry of complex oxides has a dramatic influence on their properties. Just to illustrate, two examples are the transition temperature of cuprate based high temperature superconductors and the magnetoresistance properties of $LaMnO_3$, which are changed by partially substituting La with other rare earth elements.[15]

Demanding to avoid loss of compositional control, researchers use one multielemental material source when applying, for example, pulsed laser deposition or magnetron sputter deposition.[16–19] In the latter case, it is well known that this approach does not guarantee compositional control due to the transport of the sputter particles through the sputter gas[20] and the preferential sputtering by energetic particles during thin film growth. Nevertheless, this technique is widely used in an industrial environment. However, for research applications, a multisource approach with elemental material sources gives more flexibility.[21–23] Independently of the followed synthesis technique, strategies to control and predict the composition of complex thin films are needed. As the first topic in this paper, two such strategies are demonstrated for the deposition of Mg(*M*)O films produced by dual reactive magnetron sputtering. One of these strategies is based on Monte Carlo (MC) simulations performed with the simulation code SIMTRA.[24] This seems to be the best strategy, which also gives interesting perspectives when one multielemental material source is used.[20]

The choice of MgO as a starting material is based on the large amount of data on the growth mechanism of the MgO film deposited by reactive magnetron sputtering.[25–29] This material has been used as a buffer layer in the production of so-called coated conductors, where the conducting material is a high temperature superconductor. MgO is also studied for its high electron emission yield for plasma display panels. Moreover, several interesting complex oxides contain Mg. Indeed, for the elements chosen for this study (*M* = Al, Cr, Ti, Y, and Zr), several complex oxides are discussed in literature. The well known spinel $MgAl_2O_4$ has, for example, interesting catalytic properties,[30,31] while the $MgCr_2O_4$ spinel is an important refractory material.[32] The spinel $Mg_{2-x}Ti_{1+x}O_4$ with $0 \leq x \leq 1$, is known to be a high T_c superconductor;[33] Mg–Zr–O thin films can be used as protective layers[34] and ionic conductors. ZnO is a wide band gap semiconductor used in optic and electronic device applications, which can be alloyed with MgO in order to tailor the band gap.[35] Good control of the stoichiometry combined with the flexibility of the used deposition technique enables to study the influence of the composition on the growth of MgO, and in this way, this study can be seen as a first step to understand the growth of these complex oxides.

The obtained results are compared with molecular dynamics (MD) simulations. MD simulations have been chosen as they are applicable to systems with a large number of atoms, in contrast to quantum mechanical approaches. The choice of the interatomic potential plays a crucial role in the

a)Electronic mail: marta.saraiva@ugent.be.

MD method. The experiments guided the choice of the potential in this study. Hence, the MD simulation method is used here as a powerful technique to analyze the atomistic correlations and to get more evidence for the proposed growth mechanism. Indeed, the simulations give more details about the structure as inferred from the RDF, coordination number (CN), and bond angle distribution.

The organization of the paper is based on the interplay between experiment and simulation. First, the methods used to perform the depositions (Sec. II A), the characterization of the thin films (Sec. II B), and the simulations (Sec. II C) are described. Then, the experimental and simulation results are presented and compared in Sec. III. More specifically, Sec. III A shows that the obtained composition of the deposited thin films can be predicted by binary collision MC simulations performed with the simulation code SIMTRA.[24] In Sec. III B, the experimentally determined crystallographic properties are shown and compared with the predicted properties from MD simulations. Finally, the main observations and conclusions are summarized in Sec. IV. By the comparison of experimental and simulation results, it is shown that binary collision MC and MD simulations are useful tools to control, study, and predict the composition and crystallographic properties of the deposited oxides.

II. EXPERIMENTAL CONDITIONS AND SIMULATION FRAMEWORK

A. Magnetron sputter deposition conditions

The Mg(M)O thin films were deposited by dual reactive magnetron sputtering. On one home built unbalanced planar circular magnetron, a Mg target was clamped. On a second similar magnetron, a target of the other element M (=Al, Cr, Ti, Y, and Zr) was mounted. All targets were 5 cm in diameter and 3 mm in thickness, with a purity of at least 99.95% (Kurt Lesker). The magnetrons were powered by dc supply units (Hüttinger), designed for magnetron sputtering. Each magnetron source was fixed on a linear shift, allowing in vacuum modification of the target-substrate distance. The magnetrons were mounted at 90° with respect to each other, each facing the substrate at 45°. The thin films were deposited on RCA-cleaned silicon substrates with native oxide, which were fixed on a grounded substrate holder at floating temperatures. The experimental setup is described in more detail in previous work.[36]

Different series of thin films were deposited. In each series, the composition of Mg(M)O was changed from pure MgO to pure M_xO_y. All series of thin films were deposited at a fixed argon pressure of 0.8 Pa. The discharge current for the Mg magnetron $I_{d,\mathrm{Mg}}$ was fixed at 0.5 A. For the other magnetron, it depended on the material: $I_{d,\mathrm{Cr}}=0.5$ A, $I_{d,\mathrm{Al}}=I_{d,\mathrm{Ti}}=0.7$ A, and $I_{d,\mathrm{Y}}=I_{d,\mathrm{Zr}}=0.8$ A. Depending on the used target-substrate distances, which were modified in order to achieve the desired stoichiometry, the oxygen flow was high enough to obtain fully oxidized thin films but low enough to avoid target poisoning. The deposition time was varied in order to obtain 1 μm thick films.

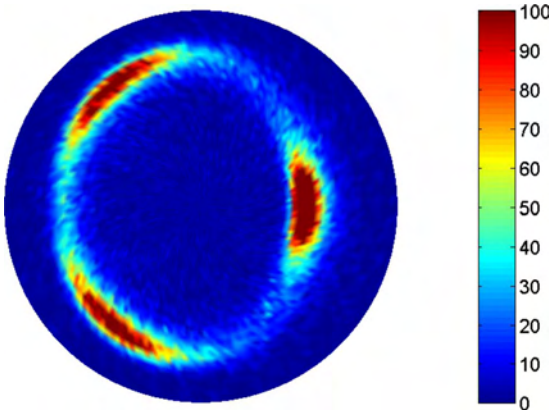

FIG. 1. (Color online) (200) pole figure of the sample with 19% of Cr (from the series Mg(Cr)O). It shows the intensity of the MgO(200) Bragg reflection as a function of the sample orientation; i.e., it gives the probability of finding the (200) crystal-plane-normal as a function of the specimen orientation. As the film has preferential (111) out-of-plane orientation, three distinct poles are noticed.

B. Thin film characterization

The thin film thickness was measured by profilometry (Talystep, Taylor-Hobson). The chemical composition was obtained using an electron probe microanalyzer (EPMA) JEOL JXA-8621MX, with a beam current of 30nA and a voltage of 15 keV. Based on the determined composition, the metal ratio is calculated as $M/(M+\mathrm{Mg})$; e.g., 19% Cr refers to a sample composition given by $Mg_{0.81}Cr_{0.19}O_{1.095}$.

The crystallographic properties were evaluated by x-ray diffraction (XRD) $\theta/2\theta$ with a LynxEye silicon strip detector mounted into a D8 discover apparatus (Bruker axs), which also has a quarter Eulerian cradle. This was used to perform the pole figure measurements in combination with a Sol-X energy dispersive x-ray detector. In these pole figures, χ (the polar angle) and φ (the azimuthal angle) were varied from 0–80° and 0–360°, respectively, in steps of 2°. An example is shown in Fig. 1.

The pole figures were used to determine the influence of the extra metal addition on the crystallinity of the thin films. However, the total number of counts in a pole figure is not directly related to the crystallinity of a thin film since the sensitivity to XRD depends on several parameters, including the angles χ and φ.[37] Hence, to retrieve a measure of the crystallinity, one needs to normalize the measured intensity. Therefore, the (200) pole figure of MgO powder was measured and used as a reference to calculate a measure of the crystallinity. Hence, this measure of the crystallinity, C, was calculated based on the MgO (200) pole figure as follows:

$$C(\mathrm{a.u.}) = \sum_{\chi=0}^{80} \sum_{\varphi=0}^{360} \frac{I_s(\chi,\varphi)}{I_p(\chi,\varphi)}, \tag{1}$$

where s corresponds to the sample, p corresponds to the powder, and $I(\chi,\varphi)$ stands for the intensity measured at the angles χ and φ.

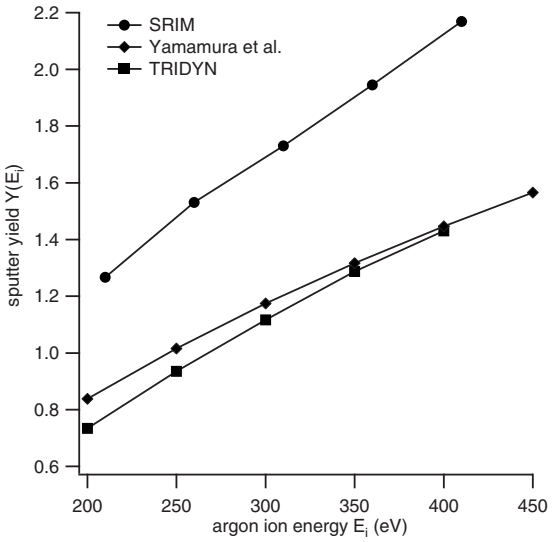

FIG. 2. The sputter yield of Cu as a function of the argon incident ion energy, calculated with different approaches.

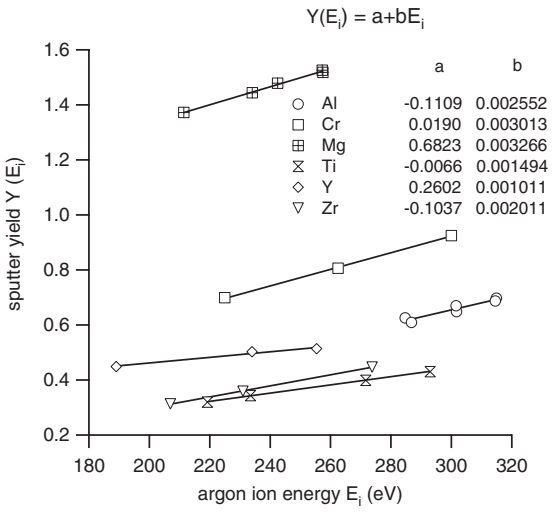

FIG. 3. Experimentally determined sputter yields for different elements. The lines are linear fits to the experimental points. The result of the linear fit is shown in the table.

C. Simulation framework

1. MC simulations

MC simulations, using the SIMTRA code,[24] were performed to predict the resulting composition of the deposited thin films. This composition depends on the used deposition conditions (discharge current I_d, target-substrate distance, total pressure, and deposition geometry) and on the sputter yield of the material for a given discharge voltage V_d. The sputter yield is the number of atoms ejected per incoming ion.

Several binary collision MC codes such as SRIM (Ref. 38) and TRIDYN (Ref. 39) are available to simulate this sputter yield. One can also use semiempirical equations such as those provided by Yamamura and Tawara.[40] Within one approach, the simulated trends are probably accurate, but as Fig. 2 shows, there is a large scatter in the calculated sputter yields by these different approaches.

In order to overcome this problem of quantification, the sputter yields to be used in the SIMTRA code for the different target materials were experimentally determined. In a magnetron discharge, the average energy of the ions bombarding the target is defined by the discharge voltage, V_d, and simulations show that this average ion energy E_i is approximately 75% of the discharge voltage.[41–43] The number of ions hitting the target can be retrieved from the discharge current, I_d, and the effective electron emission yield γ_{eff}.[44] Hence, by recording the discharge current during the sputtering of a metal target in pure argon at a constant discharge voltage, one can calculate the sputter yield at a given ion energy from the weight loss of the target, Δm, using the following equation:

$$Y(E_i) = Y(0.75V_d) = \frac{\Delta m N_A}{M \frac{I_d}{e(1+\gamma_{\text{eff}})}}, \tag{2}$$

with N_A as the Avogadro constant, e as the elementary charge, and M as the molar mass of the metal in amu.

For some materials, these experimentally determined sputter yields correspond very well to the calculated sputter yields.[41] However, for some other materials, such as Mg, strong deviations from the simulations were observed. Probably, these deviations can be attributed to a strong influence of the (sometimes unknown) surface binding energy and the unknown amount of incorporated Ar atoms in the metal target during sputtering.[45] Figure 3 gives an overview of the experimental results obtained in this study, together with a linear fit through the experimental points, which is based on the linear dependence of the sputter yield within this ion energy range.

Knowing the sputter yield and with the deposition conditions as input parameters, SIMTRA allows to calculate the flux of metallic particles toward the substrate.[24] First, the nascent energy and angular distribution of the sputtered particles leaving a metallic target are simulated with SRIM.[38] Then, the transport through an Ar gas is simulated by taking into account the collisions with the background gas. The interaction between the sputtered atoms and the background gas atoms was described by a screened Coulomb interaction potential, with a Moliere screening function.[46] Also, the thermal motion of the background gas was taken into account.[47] Since all depositions were performed in the metallic mode (the targets were not poisoned), the influence of the small partial pressure of oxygen in the vacuum chamber could be neglected.[48] The application of this simulation code for dual magnetron sputtering is shown by Bogaerts *et al.*[49] From the calculated fluxes of the sputtered atoms to the substrate, the film composition or stoichiometry at every position on the substrate can be deduced, simply based on the relative fluxes of the two different metal atoms.

2. MD simulations

The methodology used to simulate the deposition of thin films by the MD model is described in detail somewhere else.[50] The MD package DL_POLY (Ref. 51) is used to simulate the deposition of atoms. A driving program is written,

TABLE I. Short-range potential parameters used in the simulation.

i-j	*A* (eV)	*ρ* (Å)	*C* (Å^6 eV)	Ref.
Mg^{2+}–O^{2-}	1279.69	0.299 69	⋯	54
Al^{3+}–O^{2-}	1374.79	0.3013	⋯	54
Cr^{3+}–O^{2-}	1313.18	0.316 50	⋯	55
Y^{3+}–O^{2-}	1766.40	0.338 49	19.43	55
O^{2-}–O^{2-}	9547.96	0.219 16	32.0	54 and 55

which automates the deposition and relaxation. The MD method is a technique for computing the equilibrium and transport properties of a classical many-body system. Giving an initial set of positions and velocities of a system of N atoms, Newton's equations of motion are solved for this system.[52] Therefore, the reliability of the MD results is largely determined by the interatomic potential used in the simulation. In the present study, a classical pairwise ionic potential[53] describes the interactions between atoms,

$$U_{ij} = \frac{q_i q_j}{4\pi\varepsilon_0 r_{ij}} + A\exp\left(-\frac{r_{ij}}{\rho}\right) - \frac{C}{r_{ij}^6}, \tag{3}$$

where q_i and q_j are the charges of atoms i and j, r_{ij} is the distance between the atoms, and A, ρ, and C are parameters fitted for each pair of ions. The first term is the Coulomb interaction, the exponential term represents the short-range repulsion, and the term $(-r_{ij}^{-6})$ accounts for van der Waals attraction. It has been demonstrated that this potential yielded good agreement with experiments for the structure of deposited Mg(Al)O thin films.[50] Therefore, we applied the same procedure to study the deposition of Mg(Cr)O and Mg(Y)O thin films. The potential parameters used in the simulations are summarized in Table I. For all investigated systems, a rigid-ion model has been used; i.e., the ionic polarization is not considered.

Mg^{2+}, M^{3+}, and O^{2-} ions in different ratios are deposited one by one on an amorphous (Al_2O_3) substrate surface. An amorphous substrate was chosen in order to avoid possible influence of the crystalline substrate on the structure or orientation of the growing films in the simulations, as it was observed in our previous work when a MgO (100) substrate was used.[50] The simulated operating conditions, i.e., substrate temperature, initial position and velocity of the deposited ions, simulation cell size, time step, and ensembles used in the model, can be found in detail in Ref. 50. The films have been grown up to 5–8 nm thickness. This is considerably lower than the experimental film thickness but is necessary to keep the calculation time reasonable. The following $M/(M+\mathrm{Mg})$ metal ratios were investigated: 0% (i.e., a pure MgO film), 20%, 40%, 50%, 60%, 67% (i.e., the stoichiometry of the spinel structure), 80%, and 100% (i.e., a pure M_2O_3 film). The structure of the deposited thin films by the MD simulations has been defined by calculating the radial and angular (O–M–O and O–Mg–O) distribution functions (RDF and ADF, respectively) and CNs of the cations in the films.

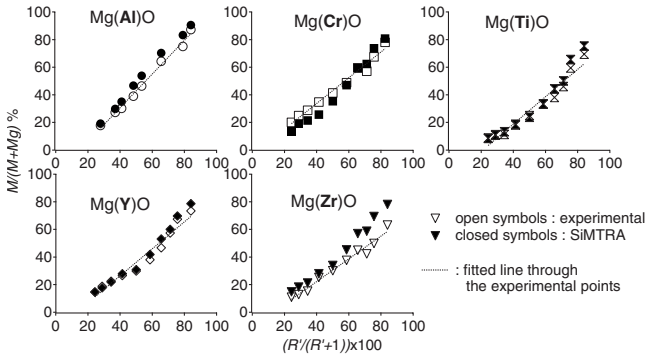

FIG. 4. Comparison of the experimental and simulated compositions $M/(M+\mathrm{Mg})$ for the different studied series. The horizontal axis refers to the relative deposition rate, as calculated from Eq. (5).

III. RESULTS AND DISCUSSION

A. Stoichiometry

To study a compositional influence, a series of Mg(M)O films was deposited with increasing concentration of M. To facilitate the experiments, two methods were used to predict the film stoichiometry under different experimental conditions.

In the first approach, we present a pure experimental method based on some simple assumptions. The composition of the deposited multielement thin film is proportional to the ratio of the material flux from source 1 to material source 2, $R=R_{d1}/R_{d2}$. Indeed, the metal ratio, defined as $M/(M+\mathrm{Mg})$, should be linearly related to

$$\frac{M}{M+\mathrm{Mg}} = \frac{R_{d1}}{R_{d1}+R_{d2}} = \frac{R}{R+1}\times 100. \tag{4}$$

In the first assumption, the deposition rate varies inversely as the square of the target-substrate distance. Hence, the ratio between the square of the target-substrate distance for both sources 1 and 2, i.e., $R'=d_2^2/d_1^2$, will be proportional to R, the ratio of the deposition rates. Based on Eq. (4), the following equation can be derived:

$$\frac{R'}{R'+\dfrac{1}{C}}, \tag{5}$$

with C the proportionality constant between R and R'. In the present work, as an approximation, the proportionality constant C was set equal to 1 for all the series. Figure 4 shows this behavior for different combinations of the Mg(M)O system. For all different series, which were performed under different conditions in discharge current and target material (with different sputter yields, angular emission profiles, and target finishing), this linear relationship holds quite well. Hence, to facilitate the deposition of multielemental oxide films, the following procedure can be followed. Two compositions are deposited under a fixed set of experimental conditions, i.e., argon pressure and discharge current. By plotting the experimentally determined compositions as a function of Eq. (5), a calibration line is retrieved (see fitted line in Fig. 4). Based on this calibration line, the relative target-substrate distances needed to deposit a given compo-

sition are determined. In this way, several compositions can be produced with a minimal number of experiments. The drawback of this method is that first two reference measurements are needed, and the method is only applicable to a given system.

Alternatively, stoichiometry can be predicted based on the SIMTRA code (see Sec. II C 1). In Fig. 4, the comparison between the composition calculated using the code (closed symbols) and the composition obtained experimentally (open symbols) for all systems is shown to be in good correspondence. The small deviations observed are within the error of the experimental composition (error in EPMA measurements) or within the error of the simulated composition (due to an error in the experimental input parameters such as discharge current, sputter yield, or statistical error of the simulations). This striking agreement between the experimental and simulated compositions indicates that SIMTRA, in combination with the correct sputter yields, allows predicting the composition of multielemental thin films deposited by dual reactive magnetron sputtering. This method is not limited by changes in the deposition geometry, or the complexity of the deposited material, as these changes can be implemented in the SIMTRA code. Of course, the predicting power of the method is limited by the correct values of the sputter yields, which were obtained experimentally in this study.

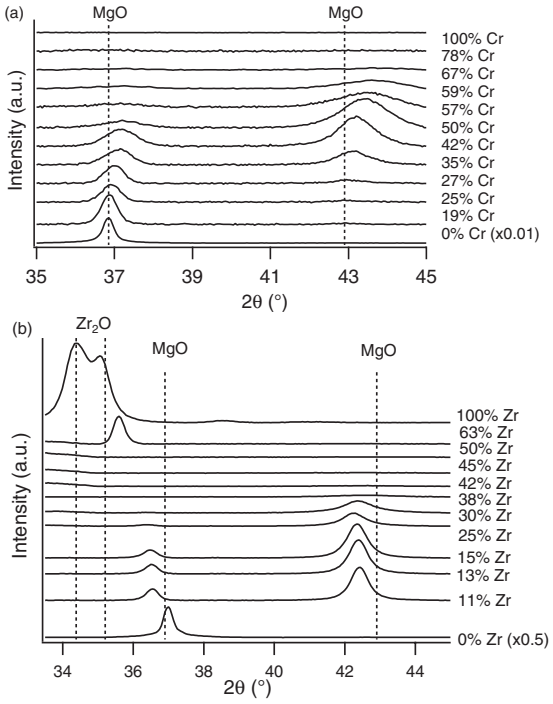

FIG. 5. XRD spectra of the (a) Mg(Cr)O and (b) Mg(Zr)O systems. The composition on the right of the graphs refers to $M/(M+\mathrm{Mg})$. The theoretical positions of the MgO peaks are marked as vertical dotted lines.

B. Crystallographic properties

1. General observations

First, the experimental and MD results are presented, and some general observations and trends are briefly mentioned. These trends will be discussed more elaborately in the next sections.

Some general observations are noticed in Figs. 5(a) and 5(b), where the $\theta/2\theta$ XRD spectra for the Mg(Cr)O and Mg(Zr)O systems are shown, respectively. It should be noted that the Mg(Cr)O system is representative of the Mg(Al)O and Mg(Ti)O systems, whereas the Mg(Zr)O system behaves similarly to the Mg(Y)O system.

Under the given experimental conditions, pure MgO thin films grow with a (111) preferential out-of-plane orientation. The mechanism resulting in this preferential orientation was the subject of previous studies and is understood in detail.[25,56] When adding another metal to MgO, two important experimental trends are noticed. The first trend is a shift of the MgO Bragg peaks compared to the peak positions in the pure MgO $\theta/2\theta$ XRD spectrum. This indicates that the lattice parameter of this phase changes by M addition. The second trend is that the crystallinity of the MgO phase decreases by the addition of another metal, which is represented by an intensity decrease of the MgO peaks in the XRD spectra. At sufficiently high concentration of the other metals, the film becomes x-ray amorphous, except for the Mg(Zr)O series, where the film becomes polycrystalline again at a Zr metal ratio higher than 63%. Although, in the Mg(Y)O series, broad peaks were found for an Y metal ratio higher than 23%, probably due to nanocrystallites. The crystallinity of the pure metal oxide depends on the material; i.e., an amorphous film was obtained for Al_2O_3, Cr_2O_3, and TiO_2, while a crystalline thin film was deposited for ZrO_2 and Y_2O_3, as reported in literature.[57–67]

Similar trends were observed in the MD simulations. Figure 6(a) shows snapshots of the simulated Mg(Cr)O thin films at different metal ratios. The thickness of the films is about 7 nm. The films at 20%, 40%, and 50% Cr metal ratio have a crystalline structure. The transition from a crystalline to an amorphous film is observed between 50% and 60% Cr metal ratios. The transition to an amorphous film in the Mg(Al)O series was found between 40% and 50% Al metal ratios.[50] Similar to the simulated Mg(Al)O previously reported,[50] the calculated pair RDFs (Mg–O, Cr–O, and O–O), O–Mg–O, and O–Cr–O ADFs indicate that the structure of the crystalline Mg(Cr)O films can be described as MgO (cubic, S.G. $Fm\bar{3}m$) with Cr in the solid solution.

Figure 6(b) shows snapshots of the simulated Mg(Y)O thin films at 20%, 40%, and 100% Y. The films at 50%, 60%, 67%, and 80% Y are very similar in structure to the film at 40% Y. It is observed that only the films at 20% and 100% Y have a crystalline structure, as well as the pure MgO (0% Y) film, as was shown in Fig. 6(a).

An illustration of analysis of the simulated film structure by the calculated pair RDFs and ADFs is given in Fig. 7 for the case of the Mg(Cr)O series. Figure 7(a) presents the calculated Mg–O RDF for the Mg(Cr)O films presented in Fig. 6(a). The Mg–O RDF in the MgO film is very similar to the corresponding RDF in the MgO relaxed crystal and can be used as a reference for the analysis of the structure of the other Mg(Cr)O films. The RDF of a crystal structure has a profile with several peaks corresponding to the lattice positions of the atoms while the RDF of an amorphous structure

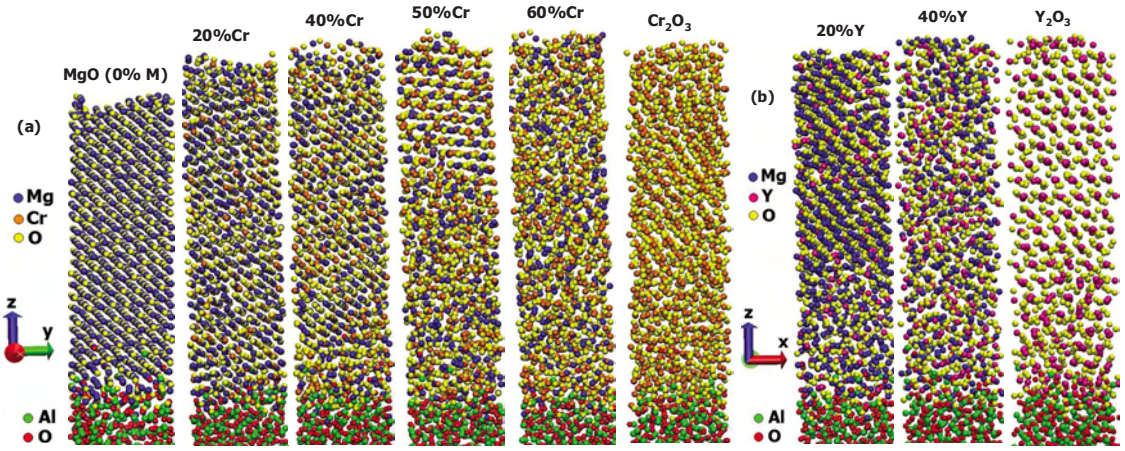

FIG. 6. (Color online) Snapshots of Mg(Cr)O (a) and Mg(y)O (b) thin films deposited by MD simulations on an amorphous Al_2O_3 substrate at different ratios of Mg, Cr/Y, and O atoms. The color code is shown.

has a profile that typically consists of one peak at the bond length between the two atoms, and further it has values close to 1. The RDFs of the films with 20%, 40%, and 50% Cr have a profile very similar to the profile of the MgO film, which represents the MgO crystal. Only the intensity of the peaks decreases with an increase in Cr concentration. The film with 60% Cr is amorphous since after the first maximum, i.e., the Mg–O bond length, the RDF has a more or less flat profile.

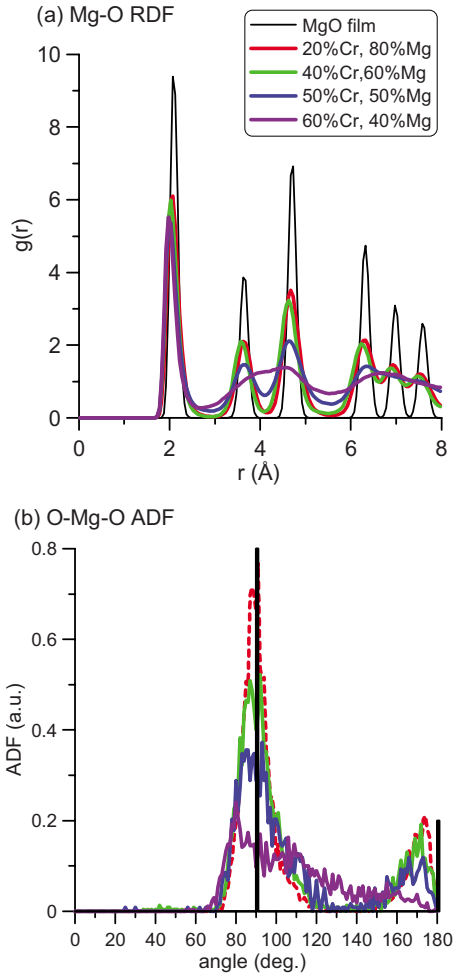

FIG. 7. (Color online) Calculated (a) Mg–O RDF and (b) O–Mg–O ADF for the Mg(Cr)O films presented in Fig. 6(a). The bold vertical lines in (b) represent the O–Mg–O bond angles in the perfect MgO crystal.

In a similar way, the O–Mg–O ADF of the films can be compared with the corresponding bond angles in the perfect MgO crystal, as shown in Fig. 7(b). Peaks close to the bond angles in the crystal show a crystalline structure, while a broad profile describes an amorphous structure. It can be observed that the intensity of the O–Mg–O ADF peaks at 90° and 180° decreases with an increase in the Cr content. The profile at 60% Cr is broad, describing an amorphous structure. In addition, the calculated CN of the cations can also contribute to determining the film structure (see Sec. III B 3).

Figure 8 shows the O–O RDFs for the Mg(M)O system for different amounts of M, for M = Al, Cr, or Y. Besides the fact that the presented RDFs show a transition from a crystalline to an amorphous structure in the three series, another feature is observed. One can clearly see that the first peak shifts toward lower values (in the case of Cr and Al) or toward higher values (in the case of Y) as the amount of M increases. Indeed, the O–O peak position shifts from 2.95 to 2.7 Å for the Mg(Al)O series, from 2.95 to 2.8 Å for the Mg(Cr)O system, and from 2.95 to 3.05 Å for the Mg(Y)O series. This indicates, similar to the experimental result, a change in the lattice parameter of the MgO phase.

In conclusion, two trends are observed in the experimental as well as in the simulation results. First, a change in the MgO lattice parameter is observed with increasing metal ratio (see Figs. 5 and 8). Second, a decrease in the crystalline MgO phase with increasing metal ratio is observed. These two trends will be discussed in more detail in the next sections.

2. Change in the MgO lattice parameter

Related to the first trend, the positions of the MgO peaks in the $\theta/2\theta$ XRD spectra enable us to calculate, using Bragg's law, the lattice parameter. Knowing this lattice parameter, also the shortest distance between two oxygen anions can be calculated based on the rocksalt (NaCl) structure of MgO. This shortest distance between two oxygen anions can also be obtained from the MD simulations because it

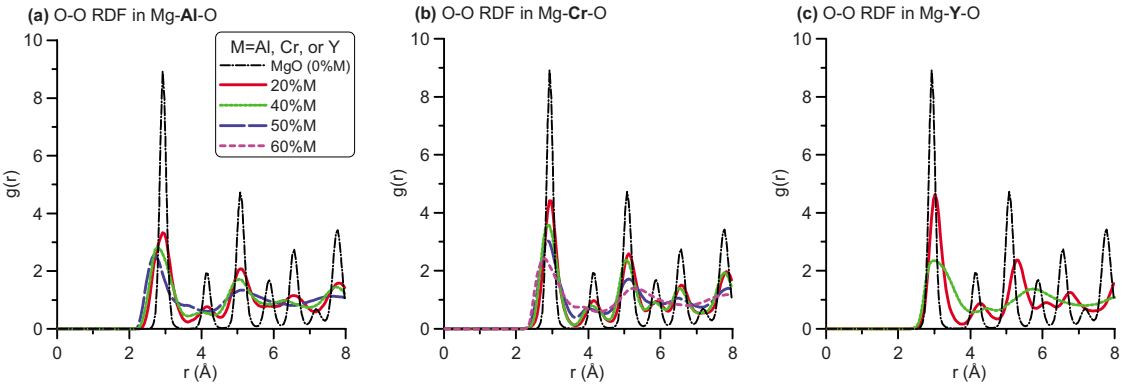

FIG. 8. (Color online) Calculated O–O RDFs for the (a) Mg(Al)O, (b) Mg(Cr)O, and (c) Mg(y)O thin films deposited by MD simulations.

corresponds to the first peak in the calculated O–O RDFs (see Fig. 8). One can clearly see from these MD simulations that the first peak shifts toward lower values (Cr and Al) or higher values (Y) as the amount of *M* increases.

A similar trend is noticed for the experimentally calculated O–O distances as it is shown in Fig. 9. This trend is known as the empirical Vegard's law, which states that the lattice parameters depend on the composition. From this behavior, one can conclude that the Mg(*M*)O systems behave as a solid solution, as already discussed by others.[68,69]

The trend is related to the cation radius, as can be concluded from the inserted table in Fig. 9. Indeed, Mg(II) has a radius of ~0.72 Å, and in a first approximation, replacing Mg by a cation with a smaller radius [such as Al(III), Cr(III), and Ti(IV)] results in a decrease in the lattice parameter, or the O–O distance. The opposite is noticed when a larger cation [such as Y(III) or Zr(IV)] replaces the Mg cation.

3. Decrease in the fraction of crystalline MgO

The second trend, as it is discussed above, is that the fraction of crystalline MgO with a NaCl phase in the thin films decreases by the addition of another metal. This crystalline fraction was determined using the procedure described in Sec. II B. Figure 10 shows the crystalline fraction of the MgO phase with a NaCl structure as a function of the composition for the different Mg(*M*)O systems. This decrease in the fraction of crystalline material in the thin films can also be deduced from the MD simulations. For example, the snapshots presented in Fig. 6 above clearly show that the crystallinity of the film decreases with increasing Cr or Y content. More quantitatively, the crystallinity could also be deduced from the calculated RDFs and ADFs shown in Figs. 7 and 8, as it was discussed in the previous section.

Added to Fig. 10 is the transition zone from crystalline to amorphous as simulated with the MD model for the Mg(Al)O, Mg(Cr)O, and Mg(Y)O systems and as deduced from the calculated RDF's. Hence, for low *M* concentrations (left side of the transition region), the calculated thin film structure is crystalline and resembles the MgO structure, while for high *M* concentrations (right side of the transition region) the structure is amorphous. Within the transition zone, the RDF peaks become broader, indicating a deviation from the crystalline MgO structure (see Figs. 7 and 8). A good correlation between experiments and MD simulation is obvious in Fig. 10.

The transition from crystalline to amorphous phases can be interpreted as follows. In case the thin films had been deposited under thermodynamical conditions, one would have observed a transition from the NaCl structure (pure MgO) over spinel ($MgAl_2O_4$) to corundum (Al_2O_3) for the Mg–Al–O series. Similar transitions would have been observed for the other series. Hence, the transition to an amorphous structure with increasing metal ratio indicates that the

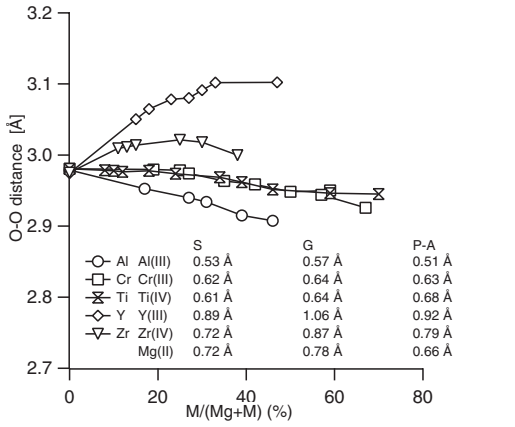

FIG. 9. O–O distances for the different Mg(*M*)O systems calculated from the $\theta/2\theta$ XRD measurements. The ionic radii were taken from Shannon (s),[70] Goldschmidt (g),[71] and the Pauling radii, which were revised and supplemented by Ahrens (P-A).[71]

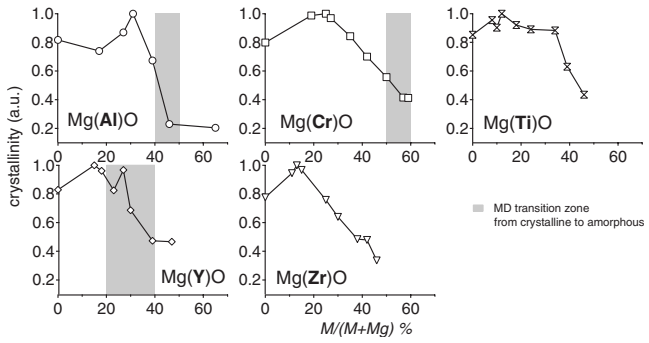

FIG. 10. Crystalline fraction of MgO [see Eq. (1)] as a function of the composition for the different Mg(*M*)O systems. The gray region represents the transition zone from crystalline to amorphous, as simulated with the MD model.

structure of the thin films is not thermodynamically but kinetically determined. This is probably caused by a too low mobility of the adatoms during the deposition.[41,56,72,73]

A good starting point to understand the metal ratio where the crystalline MgO phase disappears is a description of the MgO structure. As stated before, the MgO structure is similar to the well known NaCl structure. Hence, the O anions are in a cubic closest packing, and the Mg cations fill all octahedral sites. Therefore, the CN for Mg is 6. In a polyhedron representation, the Mg cations are within an octahedron, and the octahedra are linked by the edges; i.e., the MgO_6 octahedra share all 12 edges with adjacent octahedra. Summarizing, the MgO structure can be seen as a stable stacking of MgO octahedra.

The addition of another metal M with a higher charge than the Mg^{2+} ion will substitute Mg^{2+} in the octahedral positions. This substitution at low concentration will be compensated by vacancies on the Mg sublattice.[68,74] Based on chemical rules, i.e., the Pauling rules, one could reason as follows. The addition of the metal M will destabilize the MgO structure. First, the third Pauling rule states that the presence of shared edges in a coordinated structure decreases its stability. This effect is especially large for cations with a high valence. Second, as indicated by Vegard's law behavior, the size of the octahedra is changed, hence decreasing the stability of the octahedral stacking in the MgO structure even further. The question can now be raised as to how many Mg positions can be removed by introducing Mg vacancies and substituting the Mg positions by a different cation. Replacing Mg with a cation with the same valence but with a different size can assist in answering this latter question. For the system Mg(Zn)O (Ref. 74) and Mg(Al)O,[68] authors report a Vegard's law behavior for the lattice parameter, as also noticed for the systems discussed in this paper (see Fig. 9). A transition from the MgO structure to the ZnO wurzite structure is reported at 50% Zn/(Zn+Mg).[35,75] Hence, it seems that when half of the octahedral positions are replaced, the MgO structure becomes unstable. Building further on this idea, the number of octahedral positions in the $Mg_xM_{1-x}O_{[2x+z(1-x)]/2}$ with a rocksalt structure is equal to the number of available oxygen, i.e., $[2x+z(1-x)]/2$, with z as the charge of the substituting M ion. When $(1-x)$ M atoms are present, $z(1-x)/2$ Mg must be replaced. When this number equals half of the octahedral positions, the structure becomes unstable, i.e.,

$$\frac{z(1-x)}{2} = \frac{2x + z(1-x)}{4},$$

$$\frac{2}{2+z} = 1 - x. \tag{6}$$

For $z=2$, as in Mg(Zn)O, this would result in a transition point for $M/(Mg+M)$ at 50%, as published by several authors.[74] For $z=3$ (Cr, Al, and Y), this would set the transition point for a structural change at 2/5 or 40% $M/(M+Mg)$, while for $z=4$ (Ti and Zr) the transition should occur at 33% $M/(M+Mg)$. This corresponds more or less with the experimental and simulated results (see Fig. 10), but

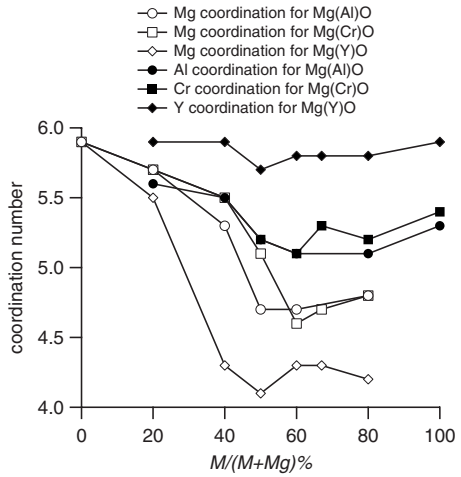

FIG. 11. Calculated CN of Mg and M (M=Al, Cr, Y) in the different systems studied by the MD simulations.

two major remarks must be given. First, it is generally accepted that the Pauling rules can only be used as guidance because it assumes a pure ionic bond between the atoms. Second, this simple reasoning does not account for any modification in the coordination of Mg, which could stabilize the structure. Indeed, the MD simulations (see Fig. 11) clearly show that the coordination of Mg deviates from 6 as in MgO with M-metal addition. Hence, the MD simulation shows that before the transition occurs, the Mg position changes toward a tetrahedral site (CN=4). This coordination is the same as in the spinel structure and shows that this transition from an octahedral to a tetrahedral site stabilizes the structure and is energetically preferred. In this way, more M can be added to the Mg(M)O structure than predicted by Eq. (6).

Nevertheless, despite these two major remarks, this simple reasoning allows to understand why the crystalline MgO phase disappears (due to the lack of mobility) and why this happens at 35%–45% $M/(M+Mg)$ (unstable structure), as was observed in the experiments as well as in the simulations.

IV. CONCLUSIONS

Several series of Mg(M)O (with M=Al, Cr, Ti, Y, and Zr) thin films were produced by dual reactive magnetron sputtering. Two different approaches to predict the stoichiometry of the deposited coatings were presented: the first one is an analytical relation that states that the deposition rate varies inversely as the square of the target-substrate distance used; the second one is based on MC simulations (SIMTRA code). The remarkable agreement verified between the experimental and simulated compositions indicates that using SIMTRA with the correct sputter yields allows the prediction of the composition of multielemental thin films.

Further, the crystallographic properties of the Mg(M)O coatings were studied and simulated by the MD method. In the experiments as well as in the simulations, two important trends were observed: a change in the MgO lattice parameters and a change in the crystalline MgO phase with increasing metal ratio. The change in the MgO lattice parameter is

in agreement with Vegard's law. The change in crystallinity was explained to be due to the lack of mobility and its vanishing at 35–45% $M/(M+\mathrm{Mg})$ due to the instability of the rocksalt structure.

In conclusion, a method to deposit complex oxide thin films with controlled stoichiometry and to investigate (experimentally and computationally) their growth has been presented and verified for Mg(M)O thin films.

ACKNOWLEDGMENTS

This work was conducted in the scope of the SBO project 60030, supported by the Institute for the Promotion of Innovation through Science and Technology in Flanders (IWT-Vlaanderen). One of the authors (S.M.) acknowledges the Research Foundation-Flanders (FWO) for financial support.

[1]P. R. Willmott, Prog. Surf. Sci. **76**, 163 (2004).
[2]E. W. Plummer, Ismail, R. Matzdorf, A. V. Melechko, and J. D. Zhang, Prog. Surf. Sci. **67**, 17 (2001).
[3]D. Levchuk, H. Bolt, M. Dobeli, S. Eggenberger, B. Widrig, and J. Ramm, Surf. Coat. Technol. **202**, 5043 (2008).
[4]J. Ramm, M. Ante, H. Brandle, A. Neels, A. Dommann, and M. Dobeli, Adv. Eng. Mater. **9**, 604 (2007).
[5]Y. L. Zhao, Z. K. Jiao, and G. H. Gao, Acta Phys. Sin. **52**, 1500 (2003).
[6]O. Auciello, J. Appl. Phys. **100**, 051614 (2006).
[7]S. Beg, N. A. S. Al-Areqi, and S. Haneef, Solid State Ionics **179**, 2260 (2008).
[8]E. Kendrick, M. S. Islam, and P. R. Slater, J. Mater. Chem. **17**, 3104 (2007).
[9]P. Laffez, X. Y. Chen, G. Banerjee, T. Pezeril, M. D. Rossell, G. Van Tendeloo, P. Lacorre, J. M. Liu, and Z. G. Liu, Thin Solid Films **500**, 27 (2006).
[10]Z. Zhuang, X. P. Wang, D. Li, T. Zhang, and Q. F. Fang, J. Am. Ceram. Soc. **92**, 839 (2009).
[11]M. S. Tomar and K. A. Kuenhold, Proceedings of the International Seminar on Current Developments in Disordered Materials, Kurukshetra, 1996, edited by D. K. Chaturvedi and G. E. Murch.
[12]A. Gies, B. Pecquenard, A. Benayad, H. Martinez, D. Gonbeau, H. Fuess, and A. Levasseur, Thin Solid Films **516**, 7271 (2008).
[13]S. W. Jin and H. N. G. Wadley, J. Vac. Sci. Technol. A **26**, 114 (2008).
[14]Z. H. Barber, J. Mater. Chem. **16**, 334 (2006).
[15]H. Y. Hwang, S. W. Cheong, P. G. Radaelli, M. Marezio, and B. Batlogg, Phys. Rev. Lett. **75**, 914 (1995).
[16]A. Erlacher, A. Ambrico, G. Perna, L. Schiavulli, T. Ligonzo, H. Jaeger, and B. Ulrich, Appl. Surf. Sci. **248**, 402 (2005).
[17]S. M. Hamidi, M. M. Tehranchi, M. Ghanaatshoar, M. Moradi, and S. M. Mohseni, J. Non-Cryst. Solids **354**, 5178 (2008).
[18]P. R. Willmott and J. R. Huber, Rev. Mod. Phys. **72**, 315 (2000).
[19]P. Barquinha, A. Pimentel, A. Marques, L. Pereira, R. Martins, and E. Fortunato, J. Non-Cryst. Solids **352**, 1749 (2006).
[20]J. Neidhardt, S. Mraz, J. M. Schneider, E. Strub, W. Bohne, B. Liedke, W. Moller, and C. Mitter, J. Appl. Phys. **104**, 063304 (2008).
[21]W. D. Sproul, D. J. Christie, and D. C. Carter, Thin Solid Films **491**, 1 (2005).
[22]W. D. Westwood, *Sputter Deposition* (AVS Monograph Editor, Ottawa, 2003).
[23]J. Musil and P. Baroch, IEEE Trans. Plasma Sci. **33**, 338 (2005).
[24]K. Van Aeken, S. Mahieu, and D. Depla, J. Phys. D: Appl. Phys. **41**, 205307 (2008).
[25]P. Ghekiere, S. Mahieu, G. De Winter, R. De Gryse, and D. Depla, J. Cryst. Growth **271**, 462 (2004).
[26]P. Ghekiere, S. Mahieu, G. De Winter, R. De Gryse, D. Depla, and O. I. Lebedev, Proceedings of the Second International Conference on Texture and Anisotropy of Polycrystals, Metz, 2005, edited by C. Esling, M. Humbert, R. A. Schwarzer, and F. Wagner, p. 433.
[27]Y. Matsuda, Y. Koyama, K. Tashiro, and H. Fujiyama, Thin Solid Films **435**, 154 (2003).
[28]C. H. Park, Y. K. Kim, S. H. Lee, W. G. Lee, and Y. M. Sung, Thin Solid Films **366**, 88 (2000).
[29]C. Young Wook and K. Jeehyun, Thin Solid Films **460**, 295 (2004).
[30]J. I. Di Cosimo, V. K. Diez, M. Xu, E. Iglesia, and C. R. Apesteguia, J. Catal. **178**, 499 (1998).
[31]S. A. Bocanegra, A. D. Ballarini, O. A. Scelza, and S. R. de Miguel, Mater. Chem. Phys. **111**, 534 (2008).
[32]N. Yoshida, Y. Takano, M. Yoshinaka, K. Hirota, and O. Yamaguchi, J. Am. Ceram. Soc. **81**, 2213 (1998).
[33]H. Hohl, C. Kloc, and E. Bucher, J. Solid State Chem. **125**, 216 (1996).
[34]G. Bingang, L. Chunliang, S. Zhongxiao, L. Liu, F. Yufeng, X. Xing, and F. Duowang, Eur. Phys. J. Appl. Phys. **36**, 111 (2006).
[35]S. Choopun, R. D. Vispute, W. Yang, R. P. Sharma, T. Venkatesan, and H. Shen, Appl. Phys. Lett. **80**, 1529 (2002).
[36]M. Saraiva, H. Chen, W. P. Leroy, S. Mahieu, N. Jehanathan, O. Lebedev, V. Georgieva, R. Persoons, and D. Depla, Plasma Processes Polym. **6**, S751 (2009).
[37]S. Mahieu, Ph.D. thesis, Ghent University, 2006.
[38]The Stopping and Range of Ions in Matter, 2006, http://www.srim.org./
[39]W. Moller, W. Eckstein, and J. P. Biersack, Comput. Phys. Commun. **81**, 355 (1988).
[40]Y. Yamamura and H. Tawara, At. Data Nucl. Data Tables **62**, 149 (1996).
[41]S. Mahieu and D. Depla, J. Phys. D: Appl. Phys. **42**, 053002 (2009).
[42]D. Czekaj, B. Goranchev, E. K. Hollmann, V. A. Volpyas, and A. G. Zaytsev, Vacuum **42**, 43 (1991).
[43]M. J. Goeckner, J. A. Goree, and T. E. Sheridan, IEEE Trans. Plasma Sci. **19**, 301 (1991).
[44]R. A. Baragiola, E. V. Alonso, J. Ferron, and A. Olivaflorio, Surf. Sci. **90**, 240 (1979).
[45]S. Mahieu, W. P. Leroy, D. Depla, S. Schreiber, and W. Moller, Appl. Phys. Lett. **93**, 061501 (2008).
[46]S. Mahieu, K. Van Aeken, and D. Depla, in *Reactive Sputter Deposition*, edited by D. Depla and S. Mahieu (Springer, New York, 2008), Vol. 109, Chap. 6.
[47]T. Nakano, I. Mori, and S. Baba, Appl. Surf. Sci. **114**, 642 (1997).
[48]S. Mahieu, G. Buyle, D. Depla, S. Heirwegh, P. Ghekiere, and R. De Gryse, Nucl. Instrum. Methods Phys. Res. B **243**, 313 (2006).
[49]A. Bogaerts, E. Bultinck, I. Kolev, L. Schwaederle, K. Van Aeken, G. Buyle, and D. Depla, J. Phys. D: Appl. Phys. **42**, 194019 (2009).
[50]V. Georgieva, M. Saraiva, N. Jehanathan, O. I. Lebelev, D. Depla, and A. Bogaerts, J. Phys. D: Appl. Phys. **42**, 065107 (2009).
[51]www.ccp5.ac.uk/DL_POLY/
[52]D. Frenkel and B. Smith, *Understanding Molecular Simulation* (Academic, New York, 2002).
[53]C. R. A. Catlow, C. M. Freeman, and R. L. Royle, Physica B & C **131**, 1 (1985).
[54]D. Bacorisen, R. Smith, J. A. Ball, R. W. Grimes, B. P. Uberuaga, K. E. Sickafus, and W. T. Rankin, Nucl. Instrum. Methods Phys. Res. B **250**, 36 (2006).
[55]K. J. W. Atkinson, R. W. Grimes, M. R. Levy, Z. L. Coull, and T. English, J. Eur. Ceram. Soc. **23**, 3059 (2003).
[56]S. Mahieu, P. Ghekiere, D. Depla, and R. De Gryse, Thin Solid Films **515**, 1229 (2006).
[57]P. Ghekiere, S. Mahieu, R. De Gryse, and D. Depla, Thin Solid Films **515**, 485 (2006).
[58]K. Koski, J. Holsa, and P. Juliet, Thin Solid Films **339**, 240 (1999).
[59]M. Sridharan, M. Sillassen, J. Bottiger, J. Chevallier, and H. Birkedal, Surf. Coat. Technol. **202**, 920 (2007).
[60]P. Hones, M. Diserens, and F. Levy, Surf. Coat. Technol. **120**, 277 (1999).
[61]S. Hong, E. Kim, D. W. Kim, T. H. Sung, and K. No, J. Non-Cryst. Solids **221**, 245 (1997).
[62]E. Aubry, P. Miska, J. Gigleux, A. Mezin, V. Demange, and A. Billard, Surf. Coat. Technol. **202**, 4980 (2008).
[63]F. M. Meng and Z. Q. Sun, Appl. Surf. Sci. **255**, 6715 (2009).
[64]R. J. Gaboriaud, F. Pailloux, P. Guerin, and F. Paumier, Thin Solid Films **400**, 106 (2001).
[65]D. Pamu, K. Sudheendran, M. G. Krishna, and K. C. J. Raju, J. Vac. Sci. Technol. A **26**, 185 (2008).
[66]K. Prabakar, A. Park, N. Cho, W. I. Lee, C. K. Hwangbo, J. G. Lee, and C. Lee, Vacuum **82**, 1367 (2008).
[67]S. Venkataraj, O. Kappertz, C. Liesch, R. Detemple, R. Jayavel, and M. Wuttig, Vacuum **75**, 7 (2004).

[68]S. Vyas, R. W. Grimes, D. J. Binks, and F. Rey, J. Phys. Chem. Solids **58**, 1619 (1997).
[69]C. L. Rohrer and G. S. Rohrer, Chem. Mater. **6**, 501 (1994).
[70]R. D. Shannon, Acta Crystallogr., Sect. A: Cryst. Phys., Diffr., Theor. Gen. Crystallogr. **32**, 751 (1976).
[71]B. F. Donald, *Crystallography and Crystal Chemistry: An Introduction* (Holt, Rinehart and Winston, New York, 1971), p. 209.
[72]P. B. Barna and M. Adamik, Thin Solid Films **317**, 27 (1998).
[73]S. Mahieu, P. Ghekiere, G. De Winter, D. Depla, R. De Gryse, O. I. Lebedev, and G. Van Tendeloo, Thin Solid Films **484**, 18 (2005).
[74]R. Kim, Y. Kim, Y. U. Lee, H. J. Kim, and J. W. Park, Surf. Coat. Technol. **161**, 52 (2002).
[75]D. Fritsch, H. Schmidt, and M. Grundmann, Appl. Phys. Lett. **88**, 134104 (2006).